frontiers | Frontiers in Earth Science

TYPE Original Research
PUBLISHED 29 May 2024
DOI 10.3389/feart.2024.1399595

OPEN ACCESS

EDITED BY
Hongjian Zhu,
Yanshan University, China

REVIEWED BY
Jian Gao,
SINOPEC Petroleum Exploration and Production Research Institute, China
Rui Yang,
China University of Geosciences Wuhan, China
Peng Qiao,
China Geological Survey, China

*CORRESPONDENCE
Zhigang Wen,
wzg728@163.com

RECEIVED 12 March 2024
ACCEPTED 17 April 2024
PUBLISHED 29 May 2024

CITATION
Wang R, Zhang Y, Chen F, Li M, Wen Z, Luo X, Ding Z, Li B and Xue Y (2024), Hydrocarbon fluid evolution and accumulation process in ultradeep reservoirs of the northern Fuman Oilfield, Tarim Basin.
Front. Earth Sci. 12:1399595.
doi: 10.3389/feart.2024.1399595

Hydrocarbon fluid evolution and accumulation process in ultradeep reservoirs of the northern Fuman Oilfield, Tarim Basin

Rujun Wang[1], Yingtao Zhang[1], Fangfang Chen[1], Mengqin Li[1], Zhigang Wen[2,3]*, Xiao Luo[1], Zhiwen Ding[1], Bing Li[1] and Yifan Xue[2,3]

[1]Tarim Oilfield Company, PetroChina, Korla, China, [2]Hubei Key Laboratory of Petroleum Geochemistry and Environment, Yangtze University, Wuhan, China, [3]Key Laboratory of Exploration Technologies for Oil and Gas Resources (Yangtze University), Ministry of Education, Wuhan, China

Marine deep Ordovician reservoirs are significantly controlled by strike-slip fault zones, which govern reservoir fluid evolution during various activity periods. Such fluid evolution elucidates the process underpinning ultra-deep oil and gas accumulation and delineates the pivotal role of strike-slip fault zones in hydrocarbon aggregation. This method can improve the understanding of the mechanism of hydrocarbon accumulation in deep to ultradeep carbonate rocks. The findings indicate that the Ordovician reservoirs in the northern thrust fault zone of the Fuman Oilfield predominantly exhibit two stages of calcite vein formation. The distribution patterns of rare earth elements and Sr isotope characteristics suggest that both stages of vein formation were sourced from Middle to Lower Ordovician marine strata, with no evidence of oxidizing fluid infiltration. This indicates that late-stage oil and gas charging in deep-ultradeep formations has good sealing properties. In these calcite veins, early-, middle-, and late-stage fluid inclusions were primarily entrapped. By examining the development of primary oil inclusions and combining the U-Pb isotope data of host minerals, this study confirms the occurrence of three stages of oil and gas charging in the deep Ordovician strata of the northern thrust fault zone in the Fuman Oilfield. These stages correspond to approximately 459 $\pm$ 7.2 Ma (mid-Caledonian), 348 $\pm$ 18 Ma (early Permian), and 268 Ma (late Permian). The key accumulation period of oil and gas reservoirs in the study area is the middle and late Caledonian, and there is a good correspondence between oil and gas charging and fault activity.

KEYWORDS

fluid inclusion, U-Pb isotope dating, fluid evolution, hydrocarbon accumulation process, ultradeep reservoirs, Tarim Basin

1 Introduction

In recent years, there have been significant breakthroughs in the exploration of deep-ultradeep carbonate reservoirs in the Tarim Basin, making it the largest production base for ultradeep oil and gas exploration and production in China (Zhu G. et al., 2021; He et al., 2023). Among these fields, the Fuman Oilfield stands out as the fastest-producing ultradeep oilfield in the deep subterranean region (Wang S. et al., 2023; Wang Q. et al., 2023). Within the thrust fault zone of the Fuman Oilfield, there is a vertical development of reservoirs primarily consisting of fractures and dissolution cavities (Zhang S. et al., 2021; Yang et al., 2021). The reservoir's fluid activity has undergone multiple stages, and the fracture veins that developed due to thrust fault zone activity record valuable information about reservoir fluid evolution (Liu et al., 2020; Liseroudi et al., 2022; Huang et al., 2023). These veins serve as indicators of fault zone fluid activity and the processes of oil and gas accumulation (Shi et al., 2017; Yu et al., 2017; Cazarin et al., 2021). The multiple phases of structural activity in the Fuman Oilfield have resulted in abundant fractures and small faults, some of which contain veins of minerals such as quartz and calcite. Observations of core samples reveal the prolific development of calcite veins within this area, often accompanied by various hydrocarbon inclusions, reflecting the multistage nature of hydrocarbon accumulation.

Building upon this, the study of the composition, temperature-pressure conditions, fluid environments, and origins of fluids in calcite veins can elucidate fluid activity in the overlapping basin (Cao et al., 2010; Nomura et al., 2014; Jia et al., 2022; Rddad et al., 2022; Wei et al., 2023). It provides evidence for the migration of fluids within source rocks and reservoirs and, to some extent, indicates the geological fluid activity patterns and the influence of structural activity on fluid movement (Yu et al., 2017; Jaya et al., 2021; Zhu et al., 2022; Fornero et al., 2023). The

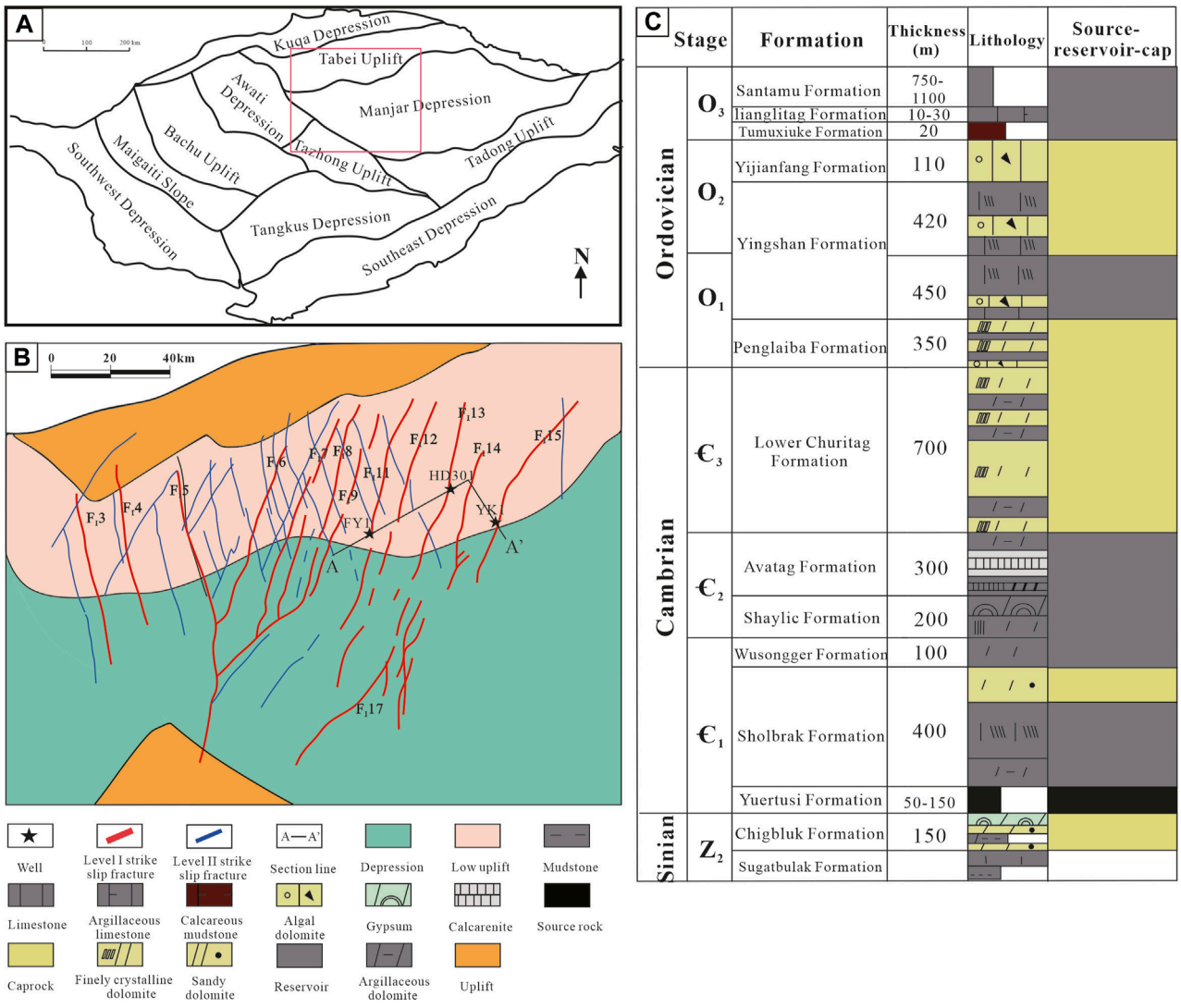

FIGURE 1
(A): Location of the Fuman Oilfield in the Tarim Basin. **(B)**: The distribution of the main faults in the lower Paleozoic strata in the Fuman Oilfield and adjacent areas. **(C)**: Stratigraphic characteristics of the lower Paleozoic carbonates in the Fuman Oilfield.

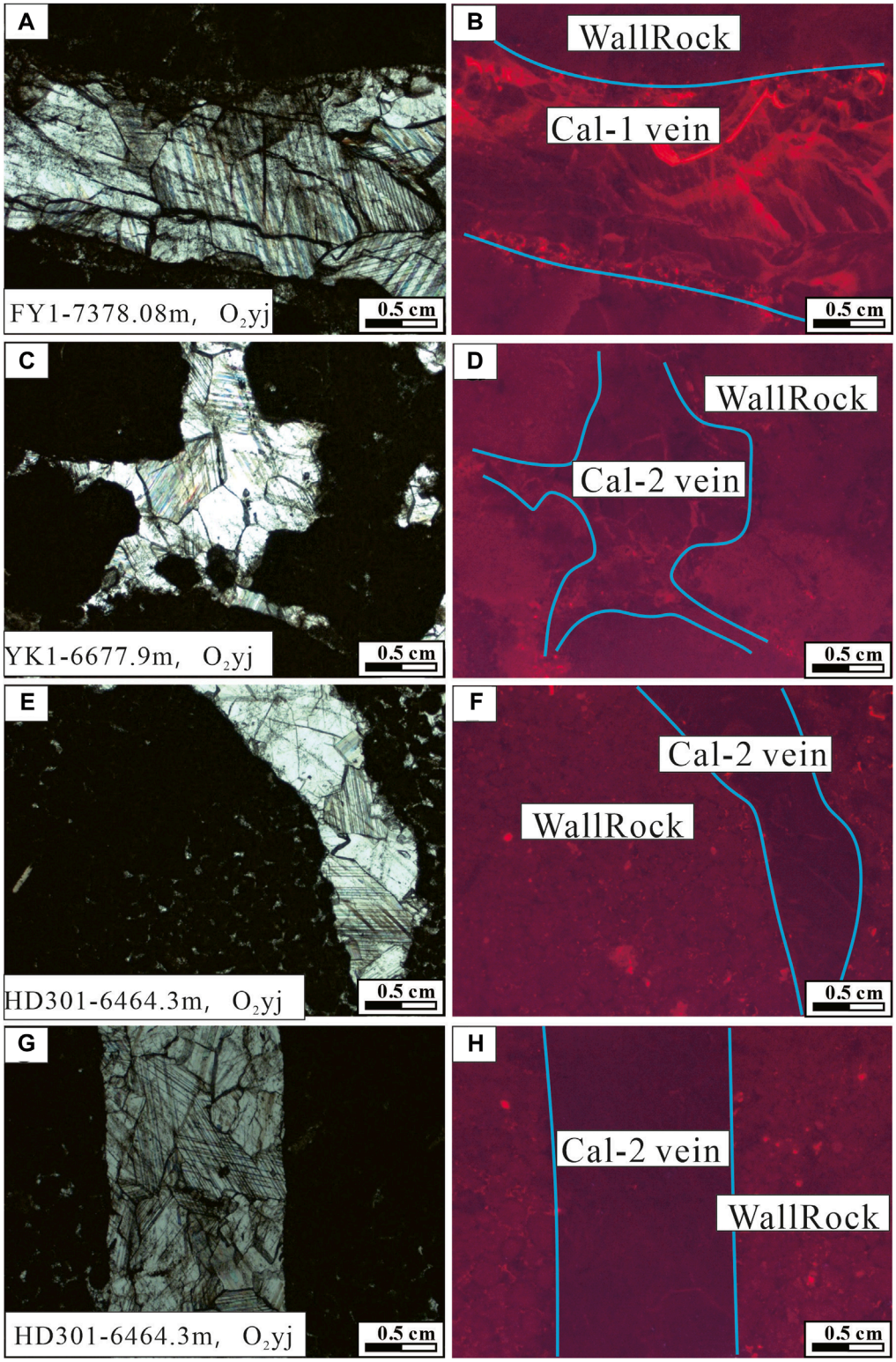

FIGURE 2
Photos showing transmission light and cathodoluminescence of representative calcite samples from the Ordovician reservoirs in the Fuman Oilfield, Tarim Basin. (A, B): Photos of transmitted light and cathodoluminescence of FY1 calcite samples. (C) and (D): Photos of transmitted light and cathodoluminescence of YK1 calcite samples. (E-H): Photos of transmitted light and cathodoluminescence of HD301 calcite samples.

TABLE 1 Rare earth element (REE) contents of different calcite veins and wall rocks of Ordovician in Fuman Oilfield, Tarim Basin.

Sample	La	Ce	Pr	Nd	Sm	Eu	Gd	Tb	Dy	Y	Ho	Er	Tm	Yb	Lu	Fe/Mn	ΣREE	δCe	δEu	LREE/HREE
Cal-1-1	0.343,984	1.796,495	0.261,676	0.241,479	0.311,572	0.178,703	0.142,874	0.119,711	0.124,417	1.026946	0.118,179	0.095508	0.067924	0.058715	0.067743	7.405,418	4.936,239	5.932,359	0.786,466	3.941,678
Cal-1-2	0.132,059	0.842,036	0.141,118	0.129,748	0.108,576	0.077431	0.087408	0.032429	0.028639	0.421,417	0.033233	0.05406	0.037077	0.032705	0.023425	6.985,077	2.171,669	6.164,751	0.790,178	4.349,769
Cal-1-3	0.126,011	1.022317	0.180,332	0.138,601	0.141,536	0.181,213	0.099947	0.059261	0.06191	0.539,099	0.06858	0.060587	0.030342	0.024984	0.031325	6.218,583	2.527,623	6.67435	1.500,836	4.096729
Wal-1-1	0.160,688	1.155,715	0.18929	0.180,241	0.17213	0.180,245	0.117,761	0.098639	0.061519	0.528,066	0.061901	0.048512	0.049491	0.047532	0.036498	17.36963	2.888,698	6.604,491	1.243,539	3.905,914
Wal-1-2	0.124,098	0.847,772	0.145,788	0.132,086	0.107,894	0.044404	0.048686	0.057626	0.048144	0.351,301	0.029203	0.013846	0.010176	0.025843	0.032172	13.76378	2.031701	6.282,455	0.567,169	5.276,859
Cal-2-1	0.013408	0.079504	0.017359	0.010218	0.013805	0	0.007297	0.003264	0.005577	0.037015	0.003746	0.005056	0	0.003231	0.000965	2.535,007	0.205,108	5.168,096	0	4.609,165
Cal-2-2	0.059626	0.294,632	0.041321	0.034341	0.023259	0.004434	0.012148	0.009761	0.001941	0.05497	0.006291	0.006675	0.003431	0.003951	0.00499	2.821,635	0.636,285	5.837,382	0.250,447	9.303,258
Cal-2-3	0.017623	0.107,567	0.023885	0.01485	0.019348	0.009489	0.009342	0.002812	0.004251	0.039754	0.007795	0.00301	0.00487	0.006953	0.001566	2.861,145	0.266,224	5.182,981	0.661,461	4.748,045
Wal-2-1	0.008208	0.055896	0.011043	0.007036	0.001894	0.020835	0.009054	0.01283	0.008454	0.045587	0.00582	0.003608	0.004349	0.003643	0	19.14613	0.167,714	5.806,989	3.805,897	2.196,751
Wal-2-2	0.008184	0.057869	0.006568	0.012215	0.002887	0.004991	0.012827	0.005012	0.004179	0.044722	0.005743	0.002384	0.010905	0.00294	0.007073	21.90835	0.175,082	7.84571	0.635,145	1.815,617

fluid inclusions in calcite veins preserve information about temperature, pressure, fluid type, and composition during mineralization, making them a crucial source of information for understanding the timing, temperature, pressure, and processes of oil and gas accumulation (Wang et al., 2020; Ping et al., 2023; Song et al., 2023; Zhou et al., 2023). Recently, a new high precision dating technique, laser *in situ* calcite U-Pb dating technique, has been developed and successfully applied to determine the exact formation age of calcite veins, effectively overcoming the error problem caused by the restrictive conditions and multiple solutions of basin simulation. This technique is important for accurately tracing the history of basin fluid activity and revealing the formation mechanism of hydrocarbon reservoirs in deep carbonate rocks under the action of multiple fluids.

This study focuses on the northern thrust fault zone of the Fuman Oilfield, utilizing analyses such as petrographic examination of calcite vein rock phases, fluorescence spectroscopy of oil inclusions, micro-area trace element analysis, Sr isotope analysis, micro-thermometry, and U-Pb isotope dating. The fluid sources and the timing of oil and gas charging in different typical well reservoir veins in the northern thrust fault zone were investigated. This research aims to reveal the controlling factors of reservoir accumulation and the role of the thrust fault zone in oil and gas accumulation from the perspective of the inherent relationship between fluid evolution and the oil and gas trapping process. This study seeks to advance our understanding of the mechanisms behind thrust fault zone reservoir formation and provide crucial theoretical support for reevaluating the distribution patterns of oil and gas in thrust fault zones.

2 Geologic setting

The Fuman Oilfield is located in the transitional zone between the Aman transitional area and the northern Tarim uplift (Figure 1). It borders the Tarim north uplift to the north and the Tarim central uplift to the south, with east-west orientations flanked by the Manjar Depression and the Awati Depression. Structurally, it exhibits an overall saddle-shaped structure and is a relatively stable tectonic unit within the basin. Based on previous analyses of the tectonic evolution of the Tarim north uplift and Tarim central uplift, as well as the activities of orogenic belts around the basin, the tectonic evolution of the Aman transitional zone likely went through several stages (Wu et al., 2019; WU et al., 2021; Gong et al., 2023). From the early Caledonian to the middle and late Hercynian, the Ammanian transition zone experienced many tectonic activities such as subsidence, extrusion and uplift. After the formation of the Alpine stage, the Ammanian transition zone settled steadily and formed the present geological pattern (Li F. et al., 2023; Li X. et al., 2023; Wang B. et al., 2023).

The Ordovician strata in the Aman transitional zone are well developed and include, from bottom to top, the Penglaiba Formation (O_1p), the Yingshan Formation ($O_{1\text{-}2}y$), the Yijianfang Formation (O_2y), the Tumuxiuke Formation (O_3t), the Lianglitag Formation (O_3l), and the Santamu Formation (O_3s). Currently, the primary target layers for exploration in the Fuman Oilfield are the 1-2 segments of the Ordovician Yijianfang Formation and the Yingshan Formation. Vertically, they are juxtaposed with the thick regional mudstones of the

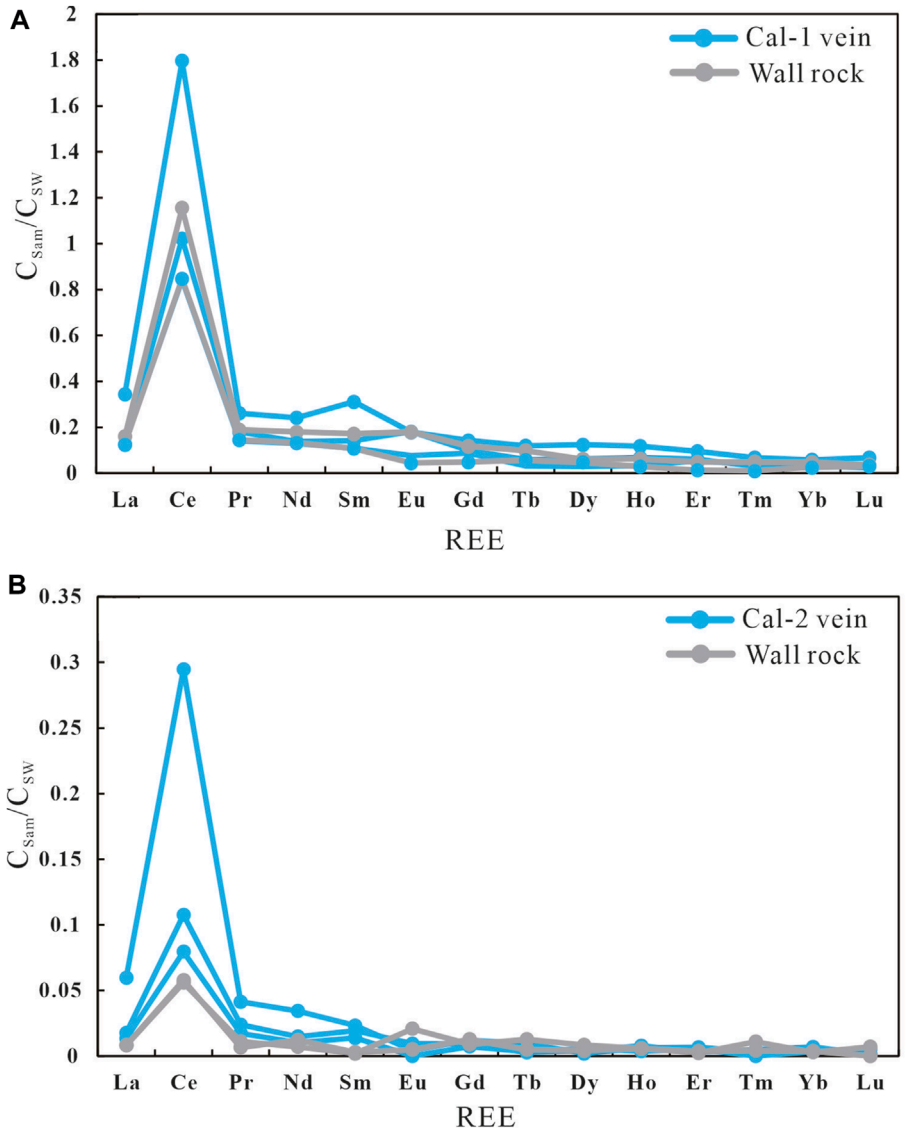

FIGURE 3
(A): Distribution pattern curve of rare earth elements in the Cal-1 veins and wall rock. **(B)**: Distribution curve of rare earth elements in the Cal-2 veins and wall rock.

Lower Cambrian Yuertusi Formation ($\epsilon_1 y$) and the Upper Ordovician Santamu Formation ($O_3 s$), forming a good source–reservoir–seal combination. Previous research has shown that in the Tarim Basin platform area, thrust faults exhibit layered differential deformation vertically. Generally, they are divided into deep and shallow structural deformation layers, with the boundary at the top surface of the Yijianfang Formation ($O_2 y$). The deep layer is characterized by upright flower-like thrust faults, while the shallow layer features a row of normal faults (Sun et al., 2023; Zhao et al., 2023). Core drilling and logging data indicate that primary pore spaces in the target layers are almost nonexistent, and the main reservoir spaces are fractures, cavities, and fissures influenced by fault-induced fracturing and karstification, resulting in fractured-vuggy reservoirs (Li W. et al., 2023; Yao et al., 2023). Unlike the typical X-shaped conjugate system in the northern Tarim Basin or the thrust-fault-controlled adjustment system in the central Tarim Basin, the Aman transitional zone lies between the two major fault systems and features a relatively low density of thrust faults in the production area (Wang P. et al., 2023). However, the Aman transitional zone experienced intense thrust fault activity, with clear profile characteristics and a series of Precambrian basement rift structures at the base. It exhibits a distinct layered deformation structure. Recent research and exploration practices have shown that the Silurian Yuertusi Formation source rocks in the Aman transitional zone have significant sediment thickness. These source rocks are overlain by thrust fault-controlled reservoirs and the thick Santamu Formation mudstone cap rock. The source rocks connect vertically through thrust faults, forming a complex thrust-fault-controlled oil and gas reservoir system with *in situ* hydrocarbon generation and vertical migration potential. This system holds immense potential for oil and gas exploration (Cao et al., 2019; Shen et al., 2019).

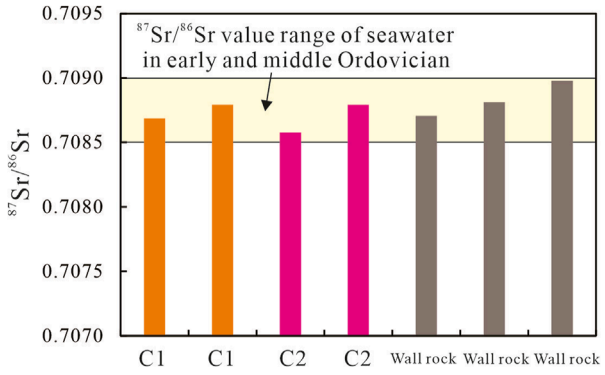

FIGURE 4
Sr isotope characteristics of calcite from Ordovician reservoirs in northern Fuman Oilfield, Tarim Basin.

3 Samples and experiments methods

3.1 Collection of cores

The experimental samples were collected from the Ordovician Yijianfang Formation carbonate reservoirs in the F_I11 fault zone of the northern Fuman Oilfield in the Tarim Basin, as well as from the HD301 well in the F_I13 fault zone and the YK1 well in the F_I15 fault zone, which are all located within the faulted zones with abundant calcite veins.

3.2 Experimental methods

3.2.1 Petrographic analysis

Micro-petrographic observation of fluid inclusions was conducted using an Olympus BX51 microscope and a Nikon-LV100 dual-channel fluorescence-transmission light microscope, and fluorescence spectra were obtained with a Maya2000Pro micro-fluorescence spectrometer. The Linkam (TH–600) heating–cooling stage was used to measure the homogenization temperatures (Th) and ice melting temperatures (Tm). The control accuracies of the Th and Tm values were ±1°C and ±0.1°C, respectively. Analysis of the cathodoluminescence (CL) characteristics of the target thin sections was performed using a CL 8200 MK5 cathodoluminescence instrument (with an accelerating voltage of 17 kV and beam current of 500 μA). Cathodoluminescence images were acquired using a Leica DM2500 microscope under the same exposure time (70 ms) and gain settings (1.005 s).

3.2.2 Microanalysis of trace elements

Microscale *in situ* elemental content analysis was carried out using a 60-micron diameter laser for ablation of carbonate veins, employing an Agilent 7700e ICP-MS instrument at Wuhan Sample Solution Analytical Technology Co., Ltd., Wuhan, China. Helium was employed as the carrier gas, and argon was utilized as the compensation gas to modulate the sensitivity during the laser ablation process. Standard samples were calibrated with multiple external standards, and no internal standard was used, employing the glass reference materials BHVO-2G, BCR-2G, and BIR-1G. Each data point of the time-resolved analysis encompassed approximately 20–30 s of the blank signal and 50 s of the sample signal. ICPMSDataCal software facilitated the correction of sample signals and the calculation of element content.

3.2.3 Sr isotope test

In situ Sr isotope measurements were performed by laser denudation multi-receiver inductively coupled plasma mass spectrometry (LA-MC-ICP-MS) using the Geolas HD laser denudation system. The laser denudation system uses helium as carrier gas and adopts single point mode. The laser beam spot size is 90 μm and the laser denudation rate is 15 Hz.

3.2.4 U-Pb dating of carbonate rocks

Carbonate rock laser *in situ* U-Pb isotope dating was conducted at the Radioisotope Laboratory, University of Queensland, Australia, utilizing an excimer laser ablation system and quadrupole inductively coupled plasma-mass spectrometry (Q-ICP-MS). After the treatment of the postcalcite pulse sample, the excimer laser was used to etch the calcite veins. The laser beam diameter measured 200 microns, with a frequency of 15 Hz and an energy density of 1.0 J/cm^2. The laser ablation material used helium as a carrier gas, while argon and nitrogen were auxiliary gases that enhanced the signal strength. The sample points encompassed 20 s of background acquisition, 25 s of data acquisition, and 10 s of sample cleaning. The standard sample NIST612's 43Ca stable isotope served as the internal standard for trace element calibration in calcite. NIST614 was primarily used for instrument sensitivity and 207 Pb/206 Pb ratio correction. AHX-1, a standard sample with an age of 209.8 Ma, mainly corrected the 238 U/206 Pb ratio. Data processing was performed with lolite v3.4 software developed by the University of Melbourne, Australia, and the generation of calcite U-Pb age harmonics maps was performed with Isoplot v.3.76 software developed by the Berkeley Center for Geochronology.

3.2.5 Basin model

By integrating the logging lithology and stratigraphic data, the burial-thermal history can be simulated by BasinMod-1D software. The measured values of the vitrinite reflectance and temperature in the borehole were all provided by the PetroChina Tarim Oilfield Company for calibrating the modeling results and are shown in Figure 8.

4 Results and discussion

4.1 Cement period of calcite veins

Within the same stratigraphic unit, fluids can exhibit significant variations in terms of oxidation-reduction conditions, fluid sources, and components during different geological periods (Guo et al., 2021). These differences indicate that the fluid information recorded by calcite veins may also vary significantly (Zhang J. et al., 2021; Muñoz-López et al., 2022). Since there is no evidence of crosscutting relationships between calcite veins in the rock samples studied, this research primarily relies on cathodoluminescence and trace element analysis to determine the formation stages of calcite

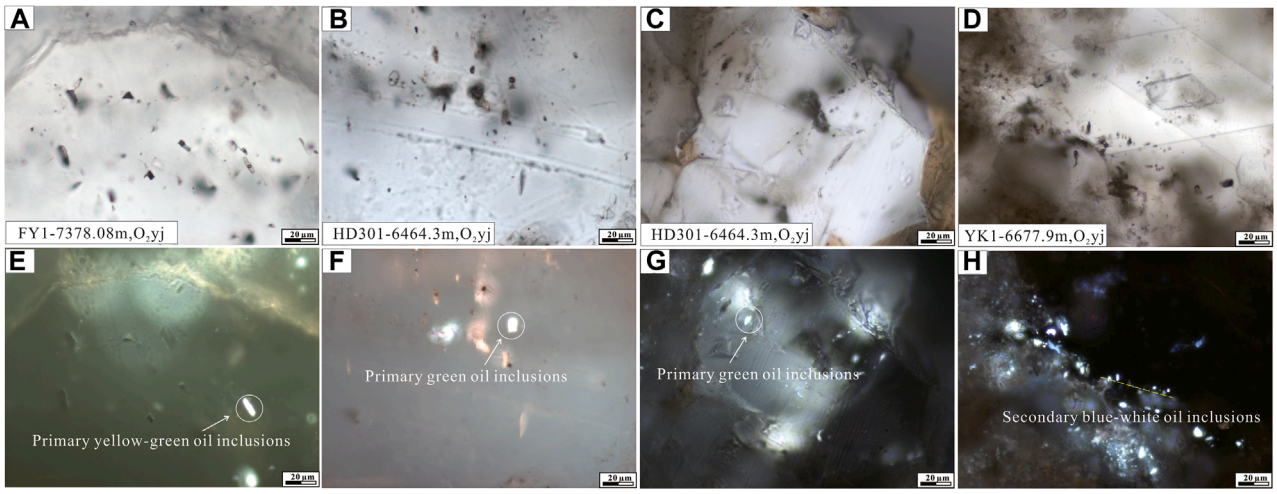

FIGURE 5
Typical micrograph of oil inclusions in calcite veins of Ordovician reservoirs in the Fuman Oilfield, Tarim Basin. **(A,E)**: Transmission light and fluorescence images of yellow–green fluorescent primary oil inclusions in the FY1 well. **(B,C,F,G)**: Transmission light and fluorescence images of green fluorescent primary oil inclusions in the HD301 well. **(D,H)**: Transmission light and fluorescence images of blue white fluorescent secondary oil inclusions in the YK1 well.

veins in different samples. The cathodoluminescence colors of calcite veins are closely related to the relative contents of Fe and Mn, and the contents of Fe and Mn are associated with the oxidation-reduction conditions of ancient fluids. Therefore, different cathodoluminescence colors of calcite veins can indicate different stages. In the Ordovician reservoirs of the northern fault zone in the Fuman Oilfield, two stages of calcite veins are primarily developed (Figure 2). The first-stage calcite vein (C1) represents fracture-fill calcite with a dark red cathodoluminescence color and Fe/Mn ratios ranging from 6.21 to 7.40 (Figures 2A, B). The second-stage calcite vein (C2) represents fractured and cavity-fill calcite with a dark brown cathodoluminescence color and Fe/Mn ratios ranging from 2.53 to 2.86 (Figures 2C–H).

4.2 Trace element characteristics

The alteration of various fluids and selective leaching of rare earth elements (REEs) in different types of rocks can significantly impact the composition of REEs in rocks, leading to distinct patterns of rare earth element distribution. In a sense, these characteristics can reflect the source and geochemical properties of the fluids (Liu et al., 2022; Wang et al., 2022). To understand the behavior of rare earth elements in calcite vein microareas in samples HD301, YK1, and FY1, they were subjected to seawater-standardized treatment (Table 1). The results are shown in Figure 3. The two stages of calcite vein formation exhibit similar rare earth element distributions, reflecting a seawater-derived distribution pattern. The total rare earth element content is relatively low, with enrichment in light rare earth elements, a flat distribution of heavy rare earth elements, and a noticeable positive anomaly in δCe values, ranging from 5.16 to 6.67 across the samples. There is no apparent positive anomaly in δEu, with values ranging from 0.25 to 1.50. These data indicate that both stages of vein formation occurred in a low-temperature fluid environment.

4.3 Sr isotope characteristics

Because strontium (Sr) has a residence time in seawater (≈1 Ma) that is much longer than the mixing time of seawater (≈1,000 a), the isotopic composition of strontium in marine environments is globally homogeneous for a given geological period. As a result, the $^{87}Sr/^{86}Sr$ ratio in seawater is a function of time over geological history (Denison et al., 1998; Han et al., 2019; Ngia et al., 2019; Ye et al., 2019), meaning that it changes with time. Therefore, it can be assumed that the isotopic composition of strontium in seawater was uniform during any specific geological period globally. In the northern region of the Fuman Oilfield, the $^{87}Sr/^{86}Sr$ values of the matrix surrounding the reservoir in the Yijianfang Formation range from 0.7087 to 0.7089, which is consistent with the early to Middle Ordovician seawater range (Figure 4). The weak cathodoluminescence intensity suggests limited interaction between the surrounding rock and fluids, indicating that there was no significant isotope exchange. Therefore, strontium isotopes can be used to trace the source of fluids. Both the C1 and C2 calcite vein bodies have $^{87}Sr/^{86}Sr$ values that fall within the range of early to Middle Ordovician seawater $^{87}Sr/^{86}Sr$ values in the Tarim Basin, ranging from 0.7085 to 0.7090. Their rare earth element patterns resemble those of seawater-derived sources. Additionally, the $^{87}Sr/^{86}Sr$ values of the veins are similar to those of the surrounding rocks. This suggests that the fluids responsible for both stages of calcite vein formation originated from the same stratigraphical (early to middle Ordovician) marine source water, and there is no evidence of oxidizing fluids infiltrating the veins, indicating good sealing during the late-stage oil and gas processes.

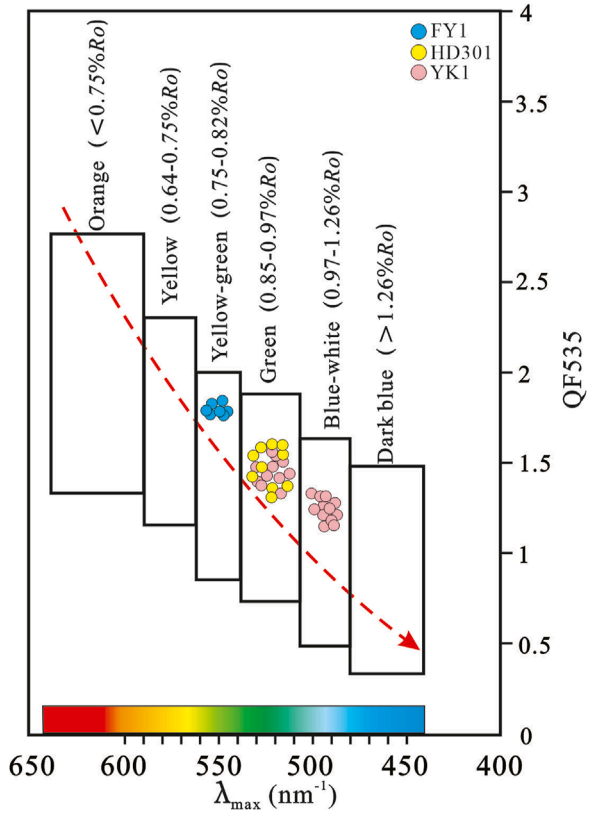

FIGURE 6
Fluorescence spectra of Ordovician oil inclusions in Fuman oilfield.

4.4 Fluid inclusion petrography

Fluid inclusions, as important tools for fluid tracing, have been widely used in the study of hydrocarbon reservoir formation and evolution (Zhou et al., 2019; Huang et al., 2023). When studying fluid inclusions, petrographic observations are crucial. Thin-section transmittance and fluorescence observations of hydrocarbon-bearing fluid inclusions in calcite veins within the northern fault zones of the Fuman Oilfield show the development of abundant primary and secondary oil inclusions (Figure 5). Primary oil inclusions are more numerous, occurring either in isolation or sporadically within the calcite veins. There are relatively few secondary oil inclusions, and they are mainly present as bead-like structures within the calcite veins or as filling structural fractures between the calcite veins and surrounding rock grains. The overall size of the oil inclusions is relatively small, typically ranging from 3 to 9 μm, with a small portion reaching 10–14 μm. In terms of shape, most are droplet-shaped or elliptical, while some exhibit irregular shapes. The differences in composition within oil inclusions result in variations in their fluorescence colors, which can be used to assess the maturity of these inclusions. As the maturity of oil inclusions increases, their fluorescence typically shifts from red to yellow to blue under ultraviolet light. Fluorescence spectral techniques under ultraviolet illumination provide a more precise means of identifying oil inclusions at different wavelengths, reducing the uncertainties associated with visual observations. Commonly used fluorescence spectral parameters include the main peak wavelength (λmax, nm) and the red-green entropy value (*QF*535, dimensionless), both of which are related to the maturity of organic matter (Kihle, 1995; Ping et al., 2019; Huang et al., 2021). In the Fuman Oilfield's northern fault zones within the Ordovician reservoirs, oil inclusion fluorescence exhibits three primary colors: yellow-green, green, and blue-white (Figure 6). The first type appears colorless to brownish under plane-polarized light and exhibits yellow-green fluorescence under ultraviolet light (Figures 5A, E). These inclusions are considered primary oil inclusions and are often sparsely distributed within calcite grains. They typically measure between 5 and 11 μm, with an elliptical shape being dominant. The λmax values are mostly within the range of 540–548 nm, and the corresponding *QF*535 values range from 1.71 to 1.94, indicating the lowest content of small molecular components in the oil inclusions and the lowest oil maturity. The second type appears colorless to brownish under plane-polarized light and exhibits green fluorescence under ultraviolet light (Figures 5B, C, F, G). These inclusions are also considered primary oil inclusions and are often sparsely or cluster-distributed within calcite grains. They typically measure between 4 and 9 μm, with some reaching 10–14 μm. They mostly have a droplet-shaped morphology, and their λmax values are mainly within the range of 512–534 nm, with corresponding *QF*535 values ranging from 1.22 to 1.68. This indicates a relatively lower content of small molecular components in the oil inclusions and lower oil maturity. The third type appears colorless under plane-polarized light and exhibits blue-white fluorescence under ultraviolet light. These inclusions are considered secondary oil inclusions (Figures 5D, H) and are primarily located within fractures in the calcite. They appear as bead-like structures, with relatively smaller sizes, mostly ranging from 3 to 8 μm. Their shapes are often irregular, and their λmax values are mainly within the range of 495–506 nm, with corresponding *QF*535 values ranging from 1.16 to 1.44. This suggests that the highest content of small molecular components occurs in the oil inclusions and has the highest oil maturity.

4.5 Micro-thermodynamics

The measurement of homogeneous temperatures in fluid inclusions is based on three fundamental assumptions: an isochoric (constant volume) system, a homogeneous system, and a closed system. During the measurement process, there may be some exceptional fluid inclusions that do not conform to these assumptions. These exceptions include instances where the gas-to-liquid ratio is excessively high, nonhomogeneous oil inclusions with abnormally high homogenization temperatures, immiscible oil and water inclusions, and extended necks, among others. After excluding fluid inclusions that are unsuitable for temperature measurement, statistical analysis is conducted on the remaining homogeneous temperatures that are considered reliable. The results are shown in Figure 7. In the Ordovician reservoir core fracture veins of well FY1, coexisting brine inclusions with yellow-green fluorescence primary oil inclusions have homogeneous temperature distributions ranging from 64.2°C to 95.6°C (Figure 7A). In the Ordovician reservoir core fracture veins of well HD301, coexisting brine inclusions with green fluorescence primary oil inclusions have

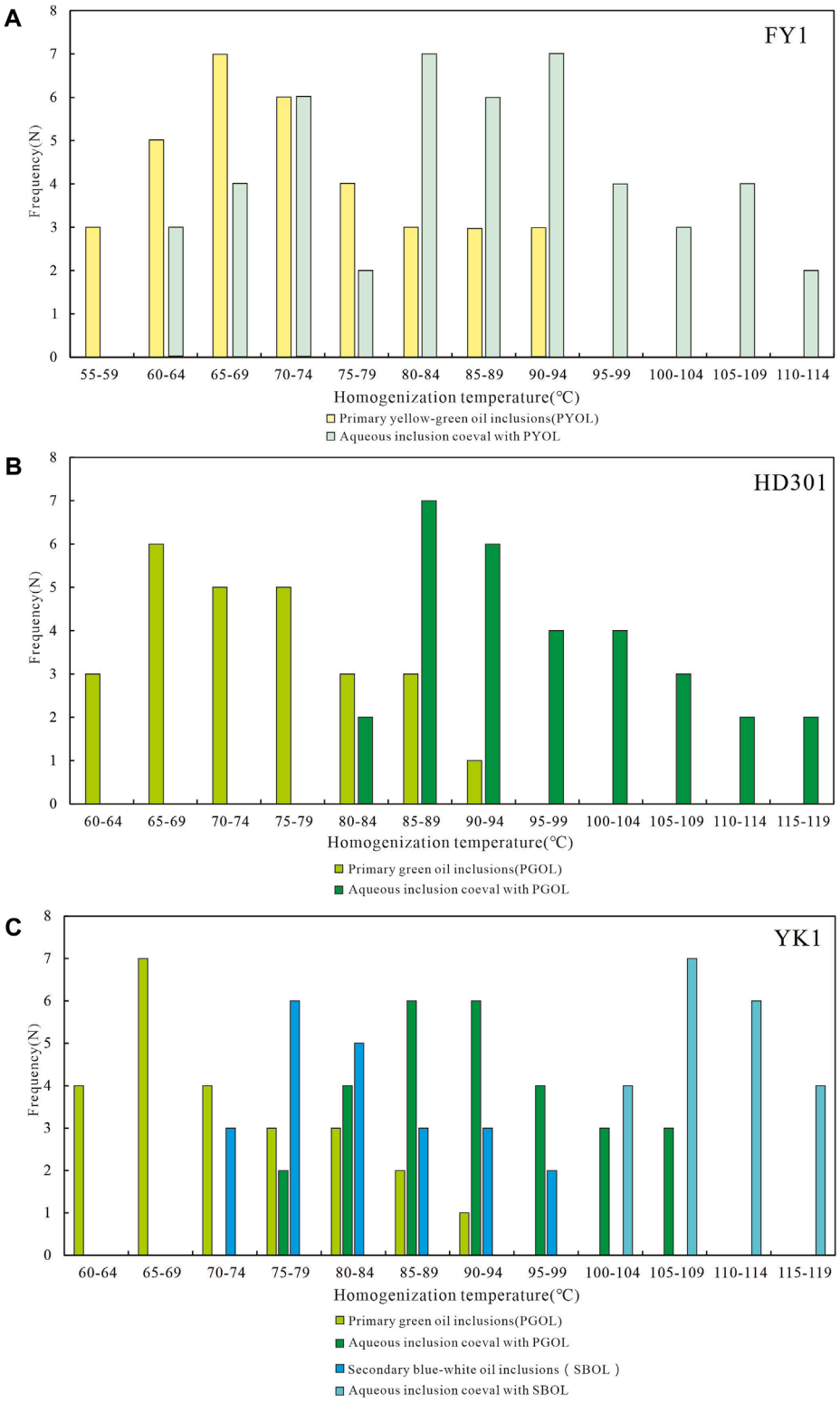

FIGURE 7
Distribution of homogenization temperatures for oil inclusions and associated aqueous inclusions in calcite veins of Ordovician reservoirs in northern Fuman Oilfield, Tarim Basin. (A): Uniform temperature distribution of oil inclusions and associated water inclusions in calcite veins of well FY1. (B): Uniform temperature distribution of oil inclusions and associated water inclusions in calcite veins of well HD301 (C): Uniform temperature distribution of oil inclusions and associated water inclusions in calcite veins of well YK1.

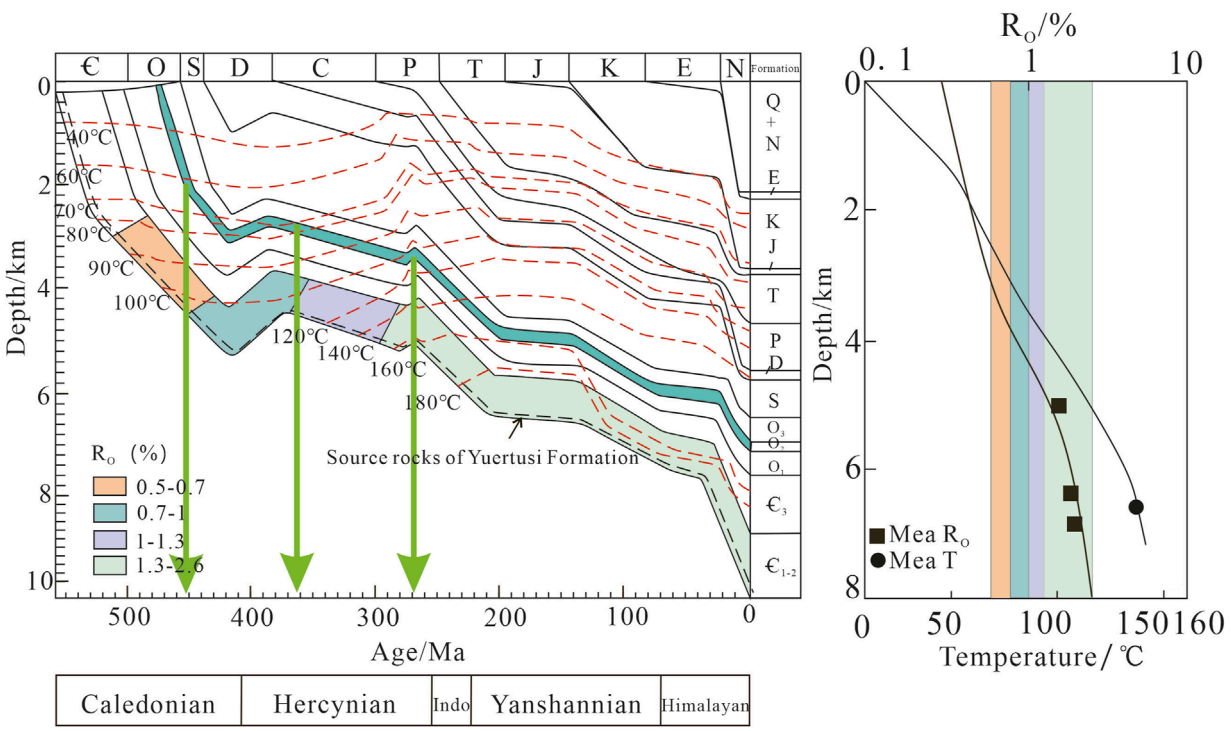

FIGURE 8
Simulation maps of burial history, thermal history and hydrocarbon generation of the strike-slip fault zone in northern Fuman Oilfield, Tarim Basin.

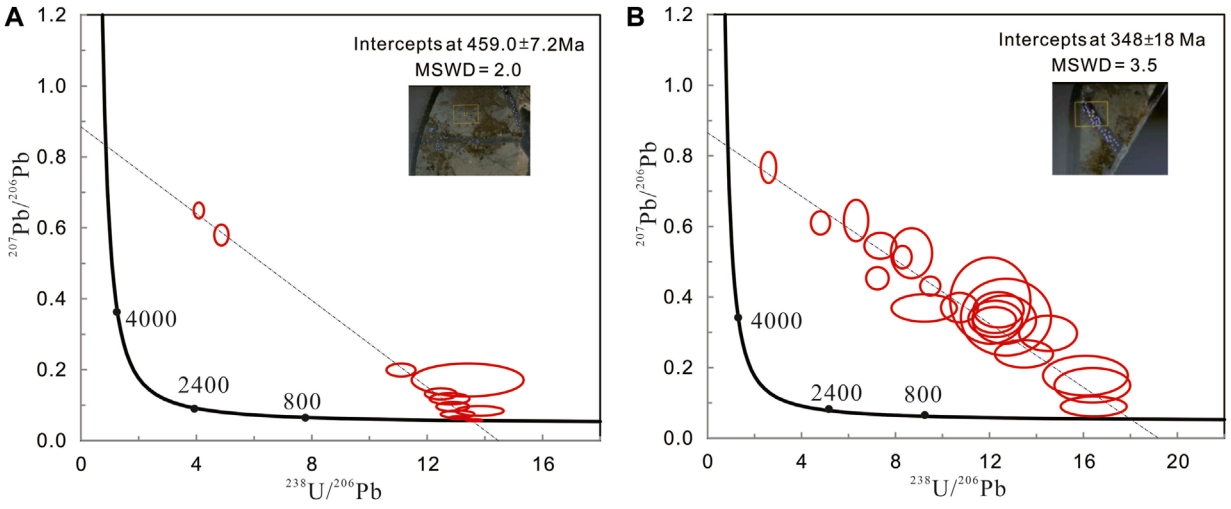

FIGURE 9
Laser *in-situ* U-Pb isotopic age of calcite veins in Ordovician reservoirs in the strike slip fault zone in northern Fuman Oilfield, Tarim Basin. (A): Laser in situ U-Pb isotope age of calcite veins in well FY1. (B): Laser in situ U-Pb isotope age of calcite veins in well HD301.

homogeneous temperature distributions ranging from 83.5°C to 118.4°C (Figure 7B). In the Ordovician reservoir core fracture veins of well YK1, coexisting brine inclusions with green fluorescence primary oil inclusions have homogeneous temperature distributions ranging from 78.2°C to 103.6°C, while coexisting brine inclusions with secondary oil inclusions with blue-white fluorescence have homogeneous temperature distributions ranging from 104.6°C to 119.3°C (Figure 7C).

4.6 Oil and gas accumulation process

Currently, the primary method for determining the timing of oil and gas accumulation is the homogenization temperature of fluid inclusions (Yang et al., 2020). This involves experimental measurements of the homogenization temperatures of fluid inclusions and their combination with the burial history and thermal evolution history of the reservoir. Based on this, by

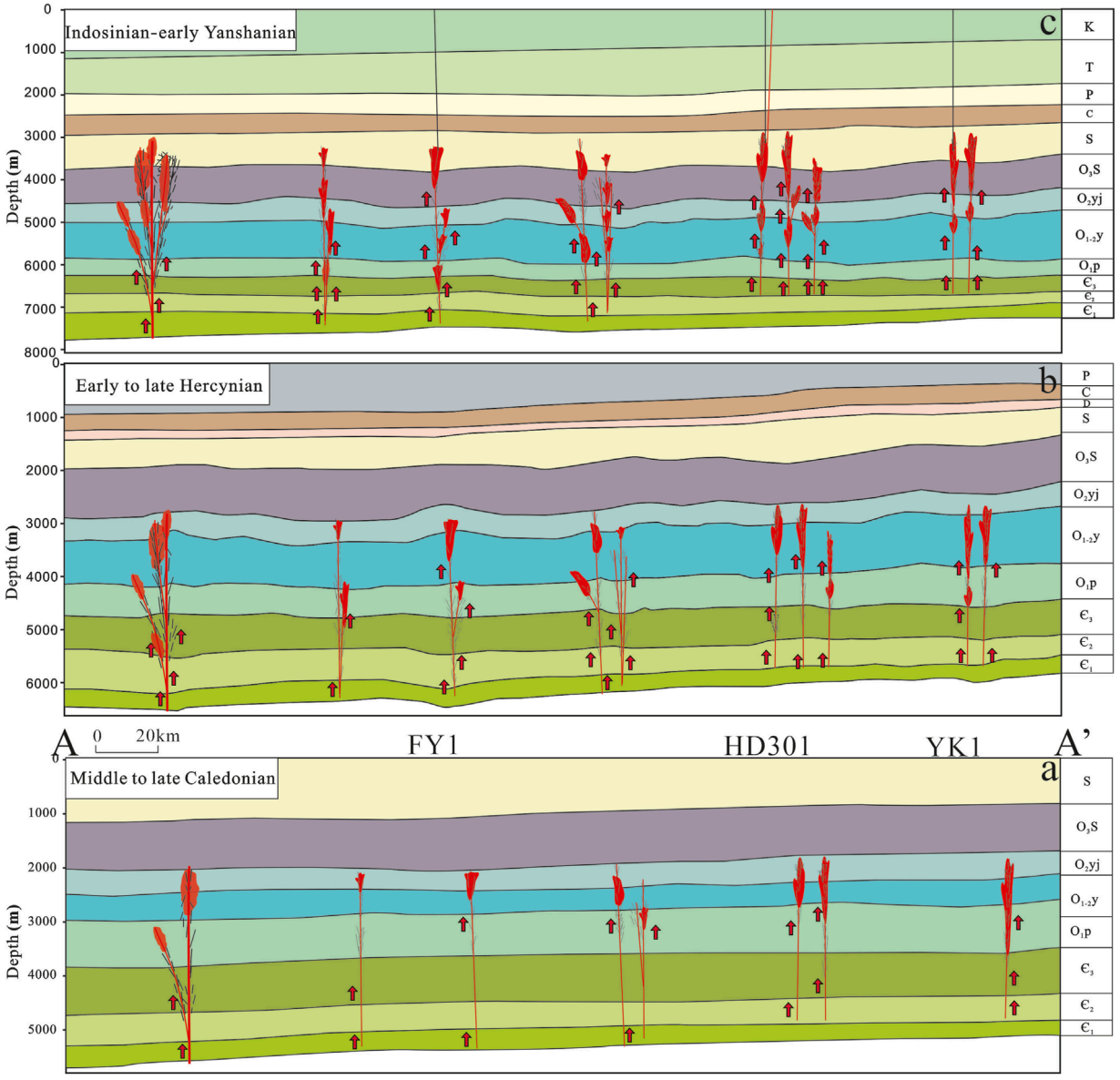

FIGURE 10
Oil and gas accumulation pattern in northern Fuman Oilfield, Tarim Basin. (A): Hydrocarbon accumulation model in northern Fuman Oilfield of Tarim Basin in middle to late Caledonian period. (B): Hydrocarbon accumulation model in northern Fuman Oilfield of Tarim Basin in early to late Hercynian period. (C): Hydrocarbon accumulation model in northern Fuman Oilfield of Tarim Basin in Indosinian to early Yanshanian period.

projecting to the corresponding temperature, geological periods of oil and gas charging can be determined. Therefore, the choice of different projection temperatures can yield different accumulation ages, making the selection of projection temperatures a key factor in improving the accuracy of oil and gas accumulation timing studies. Previous research has extensively studied fluid inclusions entrapped in carbonate rocks. During burial, especially when the paleotemperature exceeds the trapping temperature of the inclusions, the inclusions may rupture due to excessive internal pressure. This process involves stretching, fluid leakage, or refilling, resulting in a continuous increase in the homogenization temperature of the inclusions until it reaches the highest paleotemperature experienced by the formation. During these processes, the size, shape, and composition of the inclusions can affect their re-equilibration. However, in complex tectonic settings such as multicycle basins, the likelihood of later modifications is greater. Furthermore, there is inherent error in both the selection of inclusions and the measurement of homogenization temperatures. Therefore, in determining the timing of oil and gas charging in the Ordovician reservoirs of the northern fault zone of the Fuman Oilfield, selecting the minimum homogenization temperature of brine inclusions associated with oil inclusions as the projection temperature can more accurately constrain the timing of oil and gas accumulation. The entrapment time of inclusions determined using the minimum homogenization temperature of brine inclusions coexisting with oil inclusions in the

samples is shown in Figure 8. Using the minimum homogenization temperature of brine inclusions coexisting with yellow-green oil inclusions yields an estimated entrapment time of approximately 452 Ma. For green oil inclusions, the estimated entrapment time is approximately 364 Ma, and for blue-white oil inclusions, it is approximately 279 Ma. When primary hydrocarbon inclusions are developed in calcite veins, their entrapment time is consistent with the time of calcite vein formation. Thus, the ambiguity in the timing of oil and gas accumulation determined by fluid inclusion analysis can be eliminated through the absolute dating of calcite veins using U–Pb isotopes (Gladkochub et al., 2022). Laser *in situ* U-Pb dating (Figure 9) revealed that the formation age of calcite veins with primary oil inclusions in sample FY1 was 459 ± 7.2 Ma (Figure 9A), and for sample HD301, the formation age of calcite veins with primary oil inclusions was 348 ± 18 Ma (Figure 9B). This is broadly consistent with the capture times estimated using the minimum homogenization temperature of brine inclusions coexisting with oil inclusions.

The fault activity in the northern part of the Fuman oilfield in the Tarim Basin has undergone several geological periods, including the middle and late Caledonian, early to late Hercynian, and Indosinian to Yanshanian. The strike-slip fault zone first formed in the Middle Ordovician and initially presented as an upright linear fault with a relatively small scale (Figure 10A), and fracture-vuggy reservoirs were widely developed. At this time, the source rock of the Yuertusi Formation reached the hydrocarbon generation stage and began to release hydrocarbons (Cai et al., 2016; He et al., 2020; He et al., 2022a; He et al., 2022b); liquid hydrocarbons migrated upward to the Middle and Lower Ordovician strata along the vertical fracture, and a large amount of low-maturity crude oil was charged into the reservoir to form an oil reservoir. In the early Hercynian period, some tectonic uplift activities and the reactivation of strike-slip faults with a northwest strike led to the formation of new fractures and caverns, and the calcite filled with fractures and caverns broke under the action of tectonic activity (Zhu H. et al., 2021; Gao et al., 2023). At the end of the Devonian, tectonic uplift basically ended, and the source rocks of the Yuertusi Formation as a whole reached the stage of high-maturity hydrocarbon generation. High-maturity oil and gas migrated to the Ordovician reservoirs along the active strike-slip faults to accumulate (Figure 10B). Reactivity in the early Indosinian-Yanshanian fault zone provided a key transport channel for deep geological fluids and oil and gas charging. There was supplementary accumulation of oil and gas in the late Hercynian period. With the reactivation of the fault zone, deep hydrothermal fluids or organic acid fluids were able to dissolve and transform the reservoir space along the fault and fracture zone, effectively improving the reservoir space and providing a good migration channel for deep oil and gas charging (Figure 10C), which resulted in more oil and gas enrichment in the reservoir, and the scale of the oil and gas reservoirs expanded and preserved to now.

5 Conclusion

(1) Cathodoluminescence examinations indicate that the Ordovician reservoirs in the northern fault zone of the Fuman Oilfield primarily contain two stages of calcite veins. The cathodoluminescence colors observed are dark red and dark brown. The rare earth element distribution patterns and Sr isotope characteristics infer that both stages of veins originated from Middle to Lower Ordovician marine source rock fluids. There is no evidence of oxidizing fluid intrusion, indicating a good level of sealing during the late stages of deep to ultradeep oil and gas formation.

(2) In the Ordovician reservoir calcite vein samples from the northern fault zone of the Tarim Basin's Fuman Oilfield, three main stages of fluid inclusions are identified: early, middle, and late. The early-stage inclusions consist of primary oil inclusions exhibiting yellow-green fluorescence. The oil in these inclusions has relatively low maturity, with λmax values primarily falling within the range of 540–548 nm and *QF*535 values ranging from 1.71 to 1.94. The middle-stage inclusions also contain primary oil inclusions showing green fluorescence. The oil maturity in these inclusions is relatively low, with λmax values ranging from 512 to 534 nm and *QF*535 values ranging from 1.22 to 1.68. The late-stage inclusions contain secondary oil inclusions exhibiting blue-white fluorescence. These inclusions have relatively high oil maturity, with λmax values ranging primarily within the range of 495–506 nm and *QF*535 values ranging from 1.16 to 1.44.

(3) Through the observation of primary oil-bearing fluid inclusions and in conjunction with U-Pb isotopic dating of the host minerals, it has been determined that in the deep Ordovician strata of the northern fault zone of the Tarim Basin's Fuman Oilfield, there are three phases of hydrocarbon charging events. These ages correspond to approximately 459 ± 7.2 Ma (Middle Silurian), 348 ± 18 Ma (Early Permian), and 268 Ma (Late Permian). The key accumulation period of oil and gas reservoirs in the study area is the middle and late Caledonian, and there is a good correspondence between oil and gas charging and fault activity.

Data availability statement

The original contributions presented in the study are included in the article/Supplementary material, further inquiries can be directed to the corresponding author.

Author contributions

RW: Writing–review and editing. YZ: Writing–review and editing. FC: Writing–review and editing. ML: Methodology, Visualization, Writing–original draft. ZW: Funding acquisition, Writing–original draft. XL: Methodology, Visualization, Writing–original draft. ZD: Data curation, Writing–original draft. BL: Data curation, Writing–original draft. YX: Data curation, Writing–original draft.

Funding

The author(s) declare financial support was received for the research, authorship, and/or publication of this article.

Acknowledgments

We acknowledge the precious advice of the editors and reviewers. The authors thank the support from the National Natural Science Foundations of China (Nos 42302154 and 42272160) and Open Fund of Key Laboratory of Exploration Technologies for Oil and Gas Resources (Yangtze University), Ministry of Education (No. K202307).

Conflict of interest

Authors RW, YZ, FC, ML, XL, ZD, and BL were employed by Tarim Oilfield Company, PetroChina.

The remaining authors declare that the research was conducted in the absence of any commercial or financial relationships that could be construed as a potential conflict of interest.

Publisher's note

All claims expressed in this article are solely those of the authors and do not necessarily represent those of their affiliated organizations, or those of the publisher, the editors and the reviewers. Any product that may be evaluated in this article, or claim that may be made by its manufacturer, is not guaranteed or endorsed by the publisher.

References

Cai, C., Amrani, A., Worden, R. H., Xiao, Q., Wang, T., Gvirtzman, Z., et al. (2016). Sulfur isotopic composi-tions of individual organosulfur compounds and their genetic links in the Lower Paleozoic petroleum pools of the Tarim Basin, NW China. *Geochim. Cosmochim. Acta* 182, 88–108. doi:10.1016/j.gca.2016.02.036

Cao, J., Jin, Z., Hu, W., Zhang, Y., Yao, S., Wang, X., et al. (2010). Improved understanding of petroleum migration history in the Hongche fault zone, northwestern Junggar Basin (northwest China): constrained by vein-calcite fluid inclusions and trace elements. *Mar. Petrol. Geol.* 27 (1), 61–68. doi:10.1016/j.marpetgeo.2009.08.014

Cao, Y., Wang, S., Zhang, Y., Yang, M., Yan, L., Zhao, Y., et al. (2019). Petroleum geological conditions and exploration potential of lower paleozoic carbonate rocks in gucheng area, Tarim Basin, China. *Petrol. explor. Dev.* 46 (6), 1165–1181. doi:10.1016/s1876-3804(19)60271-5

Cazarin, C. L., van der Velde, R., Santos, R. V., Reijmer, J. J. G., Bezerra, F. H. R., Bertotti, G., et al. (2021). Hydrothermal activity along a strike-slip fault zone and host units in the São Francisco Craton, Brazil – implications for fluid flow in sedimentary basins. *Precambrian Res.* 365, 106365. doi:10.1016/j.precamres.2021.106365

Denison, R. E., Koepnick, R. B., Burke, W. H., and Hetherington, E. A. (1998). Construction of the cambrian and ordovician seawater 87Sr/86Sr curve. *Chem. Geol.* 152 (3), 325–340. doi:10.1016/s0009-2541(98)00119-3

Fornero, S. A., Millett, J. M., Fernandes De Lima, E., Menezes De Jesus, C., Bevilaqua, L. A., and Marins, G. M. (2023). Emplacement dynamics of a complex thick mafic intrusion revealed by borehole image log facies analyses: implications for fluid migration in the Parnaíba Basin petroleum system, Brazil. *Mar. Petrol. Geol.* 155, 106378. doi:10.1016/j.marpetgeo.2023.106378

Gao, J., Li, X., Cheng, G., Luo, H., and Zhu, H. (2023). Structural evolution and characterization of organic-rich shale from macroscopic to microscopic resolution: the significance of tectonic activity. *Adv. Geo-Energy Res.* 10 (2), 84–90. doi:10.46690/ager.2023.11.03

Gladkochub, D. P., Motova, Z. L., Donskaya, T. V., Khubanov, V. B., and Sizov, A. V. (2022). Cambrian/Ordovician boundary as a mile stone in the sedimentation history of the southern Siberian craton: evidence from U-Pb dating of detrital zircons. *J. Asian Earth Sci. X* 8, 100107. doi:10.1016/j.jaesx.2022.100107

Gong, F., Song, Y., Zeng, L., and Zou, G. (2023). The heterogeneity of petrophysical and elastic properties in carbonate rocks controlled by strike-slip fault: a case study from yangjikan outcrop in the tarim basin. *J. Petrol. Sci. Eng.* 220, 111170. doi:10.1016/j.petrol.2022.111170

Guo, R., Zhang, S., Wang, K., Han, M., and Ding, X. (2021). Multiphase dolomitization and hydrothermal alteration of the upper cambrian-lower ordovician carbonates in the gucheng uplift, Tarim Basinbasin (NW China). *J. Petrol Sci. Eng.* 206, 108964. doi:10.1016/j.petrol.2021.108964

Han, C., Lin, C., Lu, X., Tian, J., Ren, L., and Ma, C. (2019). Petrological and geochemical constraints on fluid types and formation mechanisms of the Ordovician carbonate reservoirs in Tahe Oilfield, Tarim Basin, NW China. *J. Petrol. Sci. Eng.* 178, 106–120. doi:10.1016/j.petrol.2019.03.010

He, T., Li, W., Lu, S., Pan, W., Ying, J., Zhu, P., et al. (2022a). Mechanism and geological significance of anomalous negative δ13Ckerogen in the lower cambrian, NW Tarim Basin, China. *J. Petrol. Sci. Eng.* 208, 109384. doi:10.1016/j.petrol.2021.109384

He, T., Li, W., Lu, S., Yang, E., Jing, T., Ying, J., et al. (2022b). Distribution and isotopic signature of 2-alkyl-1,3,4-trimethylbenzenes in the Lower Paleozoic source rocks and oils of Tarim Basin: implications for the oil-source correlation. *Petrol. Sci.* 19, 2572–2582. doi:10.1016/j.petsci.2022.07.014

He, T., Li, W., Lu, S., Yang, E., Jing, T., Ying, J., et al. (2023). Quantitatively unmixing method for complex mixed oil based on its fractions carbon isotopes: a case from the Tarim Basin, NW China. *Petrol. Sci.* 20, 102–113. doi:10.1016/j.petsci.2022.07.010

He, T., Lu, S., Li, W., Sun, D., Pan, W., Zhang, B., et al. (2020). Paleoweathering, hydrothermal activity and organic matter enrichment during the formation of earliest Cambrian black strata in the northwest Tarim Basin, China. *J. Petrol. Sci. Eng.* 189, 106987. doi:10.1016/j.petrol.2020.106987

Huang, Y., He, S., Guo, X., Wu, Z., Zhai, G., Huang, Z., et al. (2021). Pressure–temperature–time–composition (P–T–t–x) of paleo–fluid in Permian organic–rich shale of Lower Yangtze Platform, China: insights from fluid inclusions in fracture cements. *Mar. Petrol. Geol.* 126, 104936. doi:10.1016/j.marpetgeo.2021.104936

Huang, Y., Luo, T., Tao, Z., He, Z., Tarantola, A., He, S., et al. (2023). Fluid evolution and petroleum accumulation in the precambrian gas reservoirs of the Sichuan Basin, SW China. *Mar. Petrol. Geol.* 150, 106171. doi:10.1016/j.marpetgeo.2023.106171

Jaya, A., Nishikawa, O., Sufriadin, S., and Jumadil, S. (2021). Fluid migration along faults and gypsum vein formation during basin inversion: an example in the East Walanae fault zone of the Sengkang Basin, South Sulawesi, Indonesia. *Mar. Petrol. Geol.* 133, 105308. doi:10.1016/j.marpetgeo.2021.105308

Jia, L., Cai, C., Li, K., Liu, L., Chen, Z., and Tan, X. (2022). Impact of fluorine-bearing hydrothermal fluid on deep burial carbonate reservoirs: a case study from the Tazhong area of Tarim Basin, northwest China. *Mar. Petrol Geol.* 139, 105579. doi:10.1016/j.marpetgeo.2022.105579

Kihle, J. (1995). Adaptation of fluorescence excitation-emission micro-spectroscopy for characterization of single hydrocarbon fluid inclusions. *Org. Geochem.* 23 (11), 1029–1042. doi:10.1016/0146-6380(95)00091-7

Li, F., Lü, X., Zhu, G., Chen, J., Wang, R., Wu, Z., et al. (2023a). Formation and preservation of ultra-deep liquid petroleum in the Ordovician sedimentary succession in Tarim Basin during the neotectonic phase. *J. Asian Earth Sci.* 250, 105645. doi:10.1016/j.jseaes.2023.105645

Li, W., Xu, H., Yang, J., Gao, S., Ning, C., Yu, Y., et al. (2023c). Different depositional models of wave-dominated shoreface deposits: an integrated process-oriented analysis ("Donghe sandstones" in Tarim Basin, China). *Mar. Petrol. Geol.* 153, 106288. doi:10.1016/j.marpetgeo.2023.106288

Li, X., Zhu, G., Chen, Z., Li, T., Wang, S., Ai, Y., et al. (2023b). Mg isotopic geochemistry and origin of Early Ordovician dolomite and implications for the formation of high-quality reservoir in the Tabei area, Tarim Basin, NW China. *J. Asian Earth Sci.* 255, 105757. doi:10.1016/j.jseaes.2023.105757

Liseroudi, M. H., Ardakani, O. H., Pedersen, P. K., and Sanei, H. (2022). Fluid flow and water/rock interaction during the Early Triassic evolution of the western Canada sedimentary basin as revealed by carbonate diagenesis. *Mar. Petrol. Geol.* 142, 105765. doi:10.1016/j.marpetgeo.2022.105765

Liu, D., Zhang, C., Pan, Z., Huang, Z., Luo, Q., Song, Y., et al. (2020). Natural fractures in carbonate-rich tight oil reservoirs from the Permian Lucaogou Formation, southern Junggar Basin, NW China: insights from fluid inclusion microthermometry and isotopic geochemistry. *Mar. Petrol. Geol.* 119, 104500. doi:10.1016/j.marpetgeo.2020.104500

Liu, J., Li, Z., Wang, X., Jiang, L., Feng, Y., and Wallace, M. W. (2022). Tectonic-fluid evolution of an ultra-deep carbonate reservoir in the southern Halahatang Oilfield area, Tarim Basin, NW China. *Mar. Petrol. Geol.* 145, 105870. doi:10.1016/j.marpetgeo.2022.105870

Muñoz-López, D., Cruset, D., Vergés, J., Cantarero, I., Benedicto, A., Baqués, V., et al. (2022). U-Pb dating and geochemical dataset of fracture-filling calcite veins from the Bóixols-Sant Corneli anticline (Southern Pyrenees). *Data Brief.* 45, 108636. doi:10.1016/j.dib.2022.108636

Ngia, N. R., Hu, M., and Gao, D. (2019). Tectonic and geothermal controls on dolomitization and dolomitizing fluid flows in the Cambrian-Lower Ordovician carbonate successions in the western and central Tarim Basin, NW China. *J. Asian Earth Sci.* 172, 359–382. doi:10.1016/j.jseaes.2018.09.020

Nomura, S. F., Sawakuchi, A. O., Bello, R. M. S., Méndez-Duque, J., Fuzikawa, K., Giannini, P. C. F., et al. (2014). Paleotemperatures and paleofluids recorded in fluid inclusions from calcite veins from the northern flank of the Ponta Grossa dyke swarm: implications for hydrocarbon generation and migration in the Paraná Basin. *Mar. Petrol. Geol.* 52, 107–124. doi:10.1016/j.marpetgeo.2014.01.010

Ping, H., Chen, H., George, S. C., Li, C., and Hu, S. (2019). Relationship between the fluorescence colour of oil inclusions and thermal maturity in the Dongying Depression, Bohai Bay Basin, China: Part 2. fluorescence evolution of oil in the context of petroleum generation, expulsion and cracking under geological conditions. *Mar. Petrol. Geol.* 103, 306–319. doi:10.1016/j.marpetgeo.2019.02.024

Ping, H., Thiéry, R., Chen, H., and Liu, H. (2023). New methods to reconstruct paleo-oil and gas compositions and P-T trapping conditions of hydrocarbon fluid inclusions in sedimentary basins. *Mar. Petrol. Geol.* 155, 106403. doi:10.1016/j.marpetgeo.2023.106403

Rddad, L., Kraemer, D., Walter, B. F., Darling, R., and Cousens, B. (2022). Unravelling the fluid flow evolution and precipitation mechanisms recorded in calcite veins in relation to Pangea rifting–Newark Basin, USA. *Geochemistry-Germany* 82 (4), 125918. doi:10.1016/j.chemer.2022.125918

Shen, W., Chen, J., Wang, Y., Zhang, K., Chen, Z., Luo, G., et al. (2019). The origin, migration and accumulation of the Ordovician gas in the Tazhong III region, Tarim Basin, NW China. *Mar. Petrol. Geol.* 101, 55–77. doi:10.1016/j.marpetgeo.2018.11.031

Shi, C., Cao, J., Tan, X., Luo, B., Zeng, W., and Hu, W. (2017). Discovery of oil bitumen co-existing with solid bitumen in the Lower Cambrian Longwangmiao giant gas reservoir, Sichuan Basin, southwestern China: implications for hydrocarbon accumulation process. *Org. Geochem.* 108, 61–81. doi:10.1016/j.orggeochem.2017.03.004

Song, Y., Chen, Y., Wang, M., Steele-MacInnis, M., Ni, R., Zhang, H., et al. (2023). *In-situ* cracking of oil into gas in reservoirs identified by fluid inclusion analysis: theoretical model and case study. *Mar. Petrol. Geol.* 147, 105959. doi:10.1016/j.marpetgeo.2022.105959

Sun, J., He, J., Tao, X., Guo, S., Pan, X., Zhao, K., et al. (2023). Stratigraphic correlation and sedimentology of the Ediacaran succession in the Tarim Basin, NW China: implications for paleogeographic reconstruction and hydrocarbon exploration. *J. Asian Earth Sci.* 247, 105607. doi:10.1016/j.jseaes.2023.105607

Wang, B., Qiu, N., Littke, R., Amberg, S., and Liu, Z. (2023c). Petroleum system modelling in a compressional tectonic setting: the eastern Kuqa Depression, Tarim Basin, Northwestern China. *J. Asian Earth Sci.* 249, 105612. doi:10.1016/j.jseaes.2023.105612

Wang, P., Wang, G., Chen, Y., Hao, F., Yang, X., Hu, F., et al. (2023d). Formation and preservation of ultra-deep high-quality dolomite reservoirs under the coupling of sedimentation and diagenesis in the central Tarim Basin, NW China. *Mar. Petrol. Geol.* 149, 106084. doi:10.1016/j.marpetgeo.2022.106084

Wang, Q., Yang, H., Zhang, Y., Li, Y., Yang, X., Zhu, Y., et al. (2023b). Great discovery and its significance in the ordovician in well fudong 1 in fuman oilfield, Tarim Basin. *China Pet. Explor.* 28, 47–58. doi:10.3969/j.issn.1672-7703.2023.01.005

Wang, S., Liu, H., Deng, X., Zhu, Y., Zhang, Y., Zhao, S., et al. (2023a). Genetic mechanism of multiphase states of Ordovician oil and gas reservoirs in Fuman oilfield, Tarim Basin, China. *Mar. Petrol. Geol.* 157, 106449. doi:10.1016/j.marpetgeo.2023.106449

Wang, X., Wang, J., Cao, Y., Han, J., Wu, K., Liu, Y., et al. (2022). Characteristics, formation mechanism and evolution model of Ordovician carbonate fault-controlled reservoirs in the Shunnan area of the Shuntuogole lower uplift, Tarim Basin, China. *Mar. Petrol. Geol.* 145, 105878. doi:10.1016/j.marpetgeo.2022.105878

Wang, Y., Chang, X., Sun, Y., Shi, B., and Qin, S. (2020). Investigation of fluid inclusion and oil geochemistry to delineate the charging history of Upper Triassic Chang 6, Chang 8, and Chang 9 tight oil reservoirs, Southeastern Ordos Basin, China. *Mar. Petrol. Geol.* 113, 104115. doi:10.1016/j.marpetgeo.2019.104115

Wei, D., Gao, Z., Zhang, L., Fan, T., Wang, J., Zhang, C., et al. (2023). Application of blocky calcite vein LA-MC-ICP-MS U–Pb dating and geochemical analysis to the study of tectonic–fault–fluid evolutionary history of the Tabei Uplift, Tarim Basin. *Sediment. Geol.* 453, 106425. doi:10.1016/j.sedgeo.2023.106425

Wu, G., Lin, C., Yang, H., Liu, J., Liu, Y., Li, H., et al. (2019). Major unconformities in the mesozoic sedimentary sequences in the kuqa–tabei region, Tarim Basin, NW China. *J. Asian Earth Sci.* 183, 103957. doi:10.1016/j.jseaes.2019.103957

Wu, G., Ma, B., Han, J., Guan, B., Chen, X., Yang, P., et al. (2021). Origin and growth mechanisms of strike-slip faults in the central Tarim cratonic basin, NW China. *Petrol. explor. Dev.* 48 (3), 595–607. doi:10.1016/s1876-3804(21)60048-4

Yang, P., Wu, G., Ren, Z., Zhou, R., Zhao, J., and Zhang, L. (2020). Tectono-thermal evolution of Cambrian–Ordovician source rocks and implications for hydrocarbon generation in the eastern Tarim Basin, NW China. *J. Asian Earth Sci.* 194, 104267. doi:10.1016/j.jseaes.2020.104267

Yang, X., Tian, J., Wang, Q., Li, Y. L., Yang, H., Li, Y., et al. (2021). Geological understanding and favorable exploration fields of ultra-deep formations in Tarim Basin. *China Pet. Explor.* 26, 17–28. doi:10.3969/j.issn.1672-7703.2021.04.002

Yao, Y., Zeng, L., Mao, Z., Han, J., Cao, D., and Lin, B. (2023). Differential deformation of a strike-slip fault in the Paleozoic carbonate reservoirs of the Tarim Basin, China. *J. Struct. Geol.* 173, 104908. doi:10.1016/j.jsg.2023.104908

Ye, N., Zhang, S., Qing, H., Li, Y., Huang, Q., and Liu, D. (2019). Dolomitization and its impact on porosity development and preservation in the deeply burial Lower Ordovician carbonate rocks of Tarim Basin, NW China. *J. Petrol. Sci. Eng.* 182, 106303. doi:10.1016/j.petrol.2019.106303

Yu, Z., Liu, K., Zhao, M., Liu, S., Zhuo, Q., and Lu, X. (2017). Petrological record of hydrocarbon accumulation in the kela-2 gas field, kuqa depression, Tarim Basin. *J. Nat. Gas. Sci. Eng.* 41, 63–81. doi:10.1016/j.jngse.2017.02.034

Zhang, J., Jiang, Z., Wang, S., Wang, R., Zhang, Y., and Du, W. (2021b). Bedding-parallel calcite veins as a proxy for shale reservoir quality. *Mar. Petrol. Geol.* 127, 104975. doi:10.1016/j.marpetgeo.2021.104975

Zhang, S., Jin, Q., Sun, J., Wei, H., Cheng, F., and Zhang, X. (2021a). Formation of hoodoo-upland on Ordovician karst slope and its significance in petroleum geology in Tahe area, Tarim Basin, NW China. *Petrol Explor Dev.* 48 (2), 354–366. doi:10.1016/s1876-3804(21)60028-9

Zhao, X., Wu, C., Ma, B., Li, F., Xue, X., Lv, C., et al. (2023). Characteristics and genetic mechanisms of fault-controlled ultra-deep carbonate reservoirs: a case study of Ordovician reservoirs in the Tabei paleo-uplift, Tarim Basin, western China. *J. Asian Earth Sci.* 254, 105745. doi:10.1016/j.jseaes.2023.105745

Zhou, L., Li, Y., Jin, F., Xie, J., Pu, X., Fu, L., et al. (2023). Decipher hydrocarbon generation and accumulation based on fluid inclusion and chronology: a case study from the Upper Paleozoic buried-hills in Huanghua Depression, Bohai Bay Basin. *Petrol. Sci.* 20 (4), 1998–2008. doi:10.1016/j.petsci.2023.03.010

Zhou, X., Lü, X., Zhu, G., Cao, Y., Yan, L., and Zhang, Z. (2019). Origin and formation of deep and superdeep strata gas from Gucheng-Shunnan block of the Tarim Basin, NW China. *J. Petrol. Sci. Eng.* 177, 361–373. doi:10.1016/j.petrol.2019.02.059

Zhu, C., Gang, W., Zhao, X., Chen, G., Pei, L., Wang, Y., et al. (2022). Reconstruction of oil charging history in the multi-source petroleum system of the Beidagang buried-hill structural belt in the Qikou Sag, Bohai Bay Basin, China: based on the integrated analysis of oil-source rock correlations, fluid inclusions and geologic data. *J. Petrol. Sci. Eng.* 208, 109197. doi:10.1016/j.petrol.2021.109197

Zhu, G., Milkov, A. V., Li, J., Xue, N., Chen, Y., Hu, J., et al. (2021a). Deepest oil in Asia: characteristics of petro-leum system in the Tarim basin, China. *J. Petrol. Sci. Eng.* 199, 108246. doi:10.1016/j.petrol.2020.108246

Zhu, H., Huang, C., Ju, Y., Bu, H., Li, X., Yang, M., et al. (2021b). Multi-scale multi-dimensional characterization of clay-hosted pore networks of shale using fibsem, tem, and x-ray micro-tomography: implications for methane storage and migration. *Appl. Clay Sci.* 213, 106239. doi:10.1016/j.clay.2021.106239